

Distributed Coverage Control on Poriferous Surface via Poly-Annulus Conformal Mapping

Xun Feng, Chao Zhai, *Senior Member, IEEE*

Abstract—The inherent non-convexity of poriferous surfaces typically entraps agents in local minima and complicates workload distribution. To resolve this, we propose a distributed diffeomorphic coverage control framework for the multi-agent system (MAS) in such surfaces. First, we establish a distributed poly-annulus conformal mapping that transforms arbitrary poriferous surfaces into a multi-hole disk. Leveraging this topological equivalence, a collision-free sectorial partition mechanism is designed in the multi-hole disk, which rigorously induces strictly connected subregions and workload balance on the poriferous surfaces. This mechanism utilizes a buffer-based sequence mechanism to ensure strict topological safety when bypassing obstacles. Furthermore, a pull-back Riemannian metric is constructed to define the length metric that encodes safety constraints. Based on this metric, a distributed gradient-based control law is synthesized to drive agents toward optimal configurations, ensuring simultaneous obstacle avoidance and coverage optimization. Theoretical analyses guarantee the Input-to-State Stability (ISS) of the partition dynamics and the asymptotic convergence of the closed-loop system. Numerical simulations confirm the reachability and robustness of the proposed coverage algorithm, offering a scalable solution for distributed coverage in poriferous surfaces.

Index Terms—Coverage control, distributed control, conformal mapping, surface coverage.

I. INTRODUCTION

The rapid increase of low-cost smart agents has catalyzed significant advancements in multi-agent coordination, enabling complex missions such as environmental monitoring, cooperative search, and precision agriculture [1], [2]. Among these, coverage control stands out as a fundamental problem, aiming to optimally deploy a sensor network to monitor a field of interest with respect to a specific density function [3]. Graph theoretic methods [4] and cooperative control [5] have provided solid foundations for these tasks.

Early research extensively explores coverage control in convex domains by utilizing Voronoi tessellation to partition the region and deploying Lloyd’s algorithm to drive agents to the centroids [6], [7]. However, standard Euclidean metrics often leads to local minima in non-convex domains. To address non-convexity, Bhattacharya et al. [8] employs grid-based wavefront propagation to approximate geodesic Voronoi partitions. Nevertheless, the grid resolution limits coverage precision, thereby preventing the generation of continuous gradient

This work is supported by the “CUG Scholar” Scientific Research Funds at China University of Geosciences (Wuhan) (Project No. 2020138).

Xun Feng and Chao Zhai are with School of Automation, China University of Geosciences, Wuhan 430074, China, and with Hubei Key Laboratory of Advanced Control and Intelligent Automation for Complex Systems and also with Engineering Research Center of Intelligent Technology for Geo-Exploration, Ministry of Education (Corresponding author: Chao Zhai, email: zhaicha@amss.ac.cn).

flows on smooth manifolds. Although Bhattacharya et al [9] explore coverage on Riemannian manifolds, their approach incurs prohibitive computational costs and lacks mechanisms for workload balance. In contrast, geodesic Voronoi partitions are proposed to achieve equitable workload distribution [10]. Similarly, Palacios-Gasós et al. [11] integrate power diagrams with graph-based planning to generate sweep paths. Yet, this method requires complex geometric approximations. Sectorial partitions [12] and hierarchical protocols [13] offer alternative strategies but impose restrictive constraints on obstacle shapes. More recently, Surendhar et al. [14] integrate adaptive estimation with artificial potential fields (APF) for obstacle avoidance. Such APF-based methods are prone to trapping agents in local minima in poriferous surfaces.

To simplify the environmental topology, conformal geometry [15] offers a rigorous mathematical pathway. Caicedo-Nunez et al. [16] construct a diffeomorphism that maps physical obstacles to single points in a punctured convex region. Unfortunately, mapping solid obstacles to points induces singularities at the boundaries. Lekien and Leonard [17] utilize density-equalizing cartograms, but their diffusion-based approach is primarily limited to simply connected domains. While harmonic maps can transform workspaces into punctured disks [18], the solution to Laplace equation relies on global boundary conditions, resulting in a centralized computation process. Fan et al. [19] develop conformal navigation transformations to map obstacles into a sphere world. However, the navigation functions stabilize agents at single goal points, rendering them unsuitable for the workload balance and centroid optimization. Vlantis et al. [20] combine harmonic maps with cell decomposition, yet this requires explicit space discretization, leading to discontinuous control laws or complex switching logic between partition cells. Similarly, the neighborhood-augmented graph search [21] focuses on finding distinct paths for single robots, lacking the capacity for multi-agent workload balance. Xu et al. [22] propose time-varying diffeomorphisms for deforming domains, but it is restricted to simply connected regions and relies on centralized implementation. While combining quasi-conformal mappings with control barrier functions [24] enables reactive navigation, these methods rely on local safety constraints. Consequently, it lacks the global gradient guidance required to the optimal coverage configuration. Above all, existing methods fail to provide a distributed solution for optimal coverage with workload balance on poriferous surfaces.

To overcome these limitations, this paper proposes a fully distributed diffeomorphic coverage control framework. Inspired by the centralized multiply-connected mapping [23], we

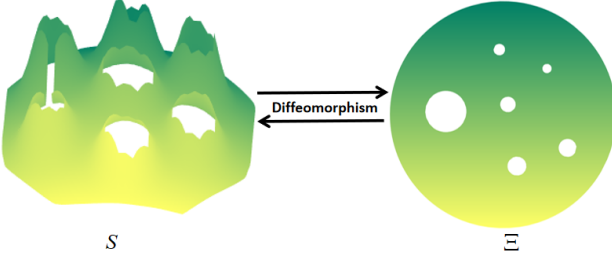


Fig. 1. Topological relationship between the surface S and n -holed disk Ξ . The color gradient illustrates the preservation of density distribution ρ .

construct a poly-annulus conformal mapping that transforms a poriferous surface into a multi-holed disk. This transformation allows to generalize the efficient sectorial partition to poriferous surfaces. Unlike traditional methods, our approach incorporates a buffer-based sequence mechanism to ensure strict topological safety. Furthermore, by utilizing partial welding techniques [25] and linear Beltrami solvers [26], we achieve this in a distributed manner. The Riemannian geometry principles [27] and classical Koebe's iteration [28] are leveraged to design a length metric that guarantees convergence. In brief, the core contributions of this work are threefold:

- 1) Construct a poly-annulus conformal mapping to regularize arbitrary poriferous surface into the multi-holed disk in a distributed manner.
- 2) Establish a modified partition mechanism to ensure strict topological safety and workload balance, which guarantees input-to-state stability of partition dynamics against geometric perturbations.
- 3) Synthesize a distributed control law that guarantees both collision-free navigation and asymptotic convergence to optimal coverage centroids by leveraging the pull-back length metric that encodes safety constraints.

The remainder of this paper is organized as follows. Section II mathematically formulates the coverage control problem on poriferous surface. Section III details the distributed construction of poly-annulus conformal mapping. Section IV presents the main theoretical results, including the safe partition algorithm, Riemannian metric design, and stability analysis. Numerical simulations are provided in Section V, and Section VI concludes the paper.

II. PROBLEM FORMULATION

This section formulates the coverage control problem of MAS on poriferous surface with boundary.

A. Mathematical Description of Coverage Region

Let S be a compact and orientable 2-dimensional Riemannian manifold with boundary embedded in \mathbb{R}^3 , which can be topologically viewed as a poly-annulus (see Fig. 1). The manifold S represents the feasible workspace constrained by a set of n disjoint obstacles, denoted as $\mathcal{O} = \{O_1, \dots, O_n\}$. Coordinating multi-agent coverage directly on S is intractable, due to the metric distortion induced by the irregular geometries of obstacle boundaries ∂O_k . As demonstrated in [24], the

problem can be simplified by mapping the robot workspace to the ball world, specifically an n -holed disk Ξ (i.e., a unit disk with radius $R = 1$, perforated by n disjoint circular obstacles). Since S is homeomorphic to Ξ , we construct a diffeomorphism $\tau : S \rightarrow \Xi$ to convert the coverage region into the ball world. As S is compact and diffeomorphism τ preserves compactness, Ξ is also compact. We define the polar coordinates in the ball world as $(\hat{r}, \hat{\theta})$ to distinguish them from those in the original robot workspace. The k -th obstacle within the ball world Ξ is uniquely characterized by its center \hat{o}_k and radius \hat{r}_k . Consequently, the feasible region of the ball world is a n -holed disk, which is defined in vector form as:

$$\Xi = \{\hat{p} \in \mathbb{R}^2 \mid \|\hat{p}\| \leq 1, \text{ s.t. } \|\hat{p} - \hat{o}_k\| > \hat{r}_k, \forall k \in \mathbb{I}_N\}, \quad (1)$$

where $\hat{p} = (\hat{r}, \hat{\theta})$ denotes the coordinate of agent in Ξ and $\mathbb{I}_N = \{1, 2, \dots, N\}$. The inequality constraints ensure that the workspace is confined within Ξ while remaining disjoint from all internal circular obstacles.

Consider a network of N agents deployed within the robot workspace S . The spatial distribution of workload is modeled by a continuous density function $\rho : S \rightarrow \mathbb{R}_{\geq 0}$. To achieve workload balance in Ξ , we transport the workload distribution to Ξ via the diffeomorphism τ . Specifically, if τ scales lengths by a conformal factor λ , the density in Ξ is given by

$$\hat{\rho}(\hat{\xi}) = \rho(\tau^{-1}(\hat{\xi})) \cdot \det(J_{\tau^{-1}}(\hat{\xi})), \quad \forall \hat{\xi} \in \Xi, \quad (2)$$

where $J_{\tau^{-1}}(\hat{\xi})$ denotes the Jacobian of τ^{-1} . Note that the density within the obstacle regions is defined as zero. The sectorial partition can be implemented to divide the region Ξ and balance the workload of subregions [13]. Each agent is assigned with a virtual partition bar, parameterized by an angular phase $\hat{\psi}_i \in [0, 2\pi]$. And the partition phases are numbered sequentially as $0 \leq \hat{\psi}_1 < \hat{\psi}_2 < \dots < \hat{\psi}_N < 2\pi$. Consequently, the ball world is decomposed into N sectors $\Xi = \bigcup_{i=1}^N \hat{E}_i$, where \hat{E}_i is the region bounded by the angles $[\hat{\psi}_i, \hat{\psi}_{i+1}]$. The dynamics of the i -th agent is presented as

$$\dot{\mathbf{p}}_i = \mathbf{u}_i \quad (3)$$

with the control input $\mathbf{u}_i \in T_{p_i} S$, $\forall i \in \mathbb{I}_N = \{1, 2, \dots, N\}$. While agents operate in the robot workspace S , the partition dynamics is computed in the ball world Ξ . Concretely, the workload \hat{m}_i in Ξ is calculated by

$$\hat{m}_i = \int_{\hat{\psi}_i}^{\hat{\psi}_{i+1}} \hat{\omega}(\hat{\theta}) d\hat{\theta}, \quad \hat{\omega}(\hat{\theta}) = \int_0^1 \hat{\rho}(\hat{r}, \hat{\theta}) \hat{r} d\hat{r}, \quad (4)$$

where $\hat{\omega}(\hat{\theta})$ represents the marginal density along the angular coordinate in Ξ . In addition, the radial integration is performed over $[0, 1]$, as the density $\hat{\rho}$ vanishes within the internal obstacles. To balance the workload among subregions, the dynamic of the i -th partition bar in Ξ is designed as

$$\dot{\hat{\psi}}_i = k_{\hat{\psi}}(\hat{m}_i - \hat{m}_{i-1}), \quad \forall i \in \mathbb{I}_N, \quad (5)$$

where $k_{\hat{\psi}}$ is a positive constant, and $\hat{\psi}_i = \text{mod}(\hat{\psi}_i, 2\pi)$ is employed to ensure $\hat{\psi}_i \in [0, 2\pi]$ with periodic boundary conditions $\hat{\psi}_{N+1} = \hat{\psi}_1 + 2\pi$ and $\hat{m}_0 = \hat{m}_N$.

B. Optimization Formulation for Multi-Agent Coverage

To rigorously quantify the coverage performance, we define a global cost function directly in the robot workspace S . Inspired by the distortion energy framework in [6], the performance index is formulated as

$$J(\hat{\psi}, \mathbf{p}) = \sum_{i=1}^N \int_{E_i(\hat{\psi})} f_i(d_l(p_i, q)) \rho(q) dq, \quad (6)$$

where $\mathbf{p} = (p_1, \dots, p_N)^T$ denotes the position vector of agents in S , and $\hat{\psi} = (\hat{\psi}_1, \dots, \hat{\psi}_N)^T$ represents the vector of partition phase angles in ball world Ξ , which determines the workspace subregions via the inverse mapping $E_i(\hat{\psi}) = \tau^{-1}(\hat{E}_i(\hat{\psi}))$. In addition, $d_l(p_i, q)$ refers to the length metric designed in Subsection IV-B1 to encode obstacle avoidance. To ensure the well-posedness of the performance index (6), $f_i(\cdot)$ satisfies the following assumption [10].

Assumption II.1 (Admissible Performance Functions). *We require $f_i(\cdot)$ to satisfy:*

- 1) $f_i \in C^2([0, \infty))$.
- 2) $f_i'(x) > 0$ and $f_i''(x) > 0$ for all $x \geq 0$.
- 3) $f_i(0) = 0$ and $\lim_{x \rightarrow \infty} f_i(x) = \infty$.

A standard example satisfying these criteria is $f(x) = x^2$.

Our objective is to optimize coverage performance with workload balance over the robot workspace S . Since the diffeomorphism τ establishes a topological equivalence between the two domains, solving the coverage problem in the robot workspace S is equivalent to solving its counterpart in the ball world Ξ . (see Theorem IV.2). Specifically, we design a distributed control law for the agent dynamics (3) in S that utilizes the partition dynamic (5) in Ξ to drive agents toward their optimal positions. Inspired by the coverage framework in [10], the optimization problem is formulated as follows:

$$\begin{aligned} & \min_{\hat{\psi}, \mathbf{p}} J(\hat{\psi}, \mathbf{p}) \\ \text{s.t. } & |\hat{m}_i - \hat{m}_j| \leq \delta(\beta), \quad \forall i, j \in \mathbb{I}_N \end{aligned} \quad (7)$$

where $\delta(\beta)$ represents the workload deviation arising from topological safety constraints. The primary challenge of Problem (7) stems from the non-convexity and complex topology of the workspace. Our framework addresses these challenges by regularizing the workspace topology within the ball world while utilizing the conformal mapping and the pull-back length metric to ensure physical fidelity.

III. CONSTRUCTION OF CONFORMAL MAPPING

This section details the construction of poly-annulus conformal mapping $\tau : S \rightarrow \Xi$. We employ a partition operator \mathcal{P} to decouple S into subdomains, reducing the global mapping into parallelizable local sub-problems. These local maps are integrated via partial welding and geometric rectification to yield a n -holed disk suitable for sectorial partition.

A. Domain Decomposition

To facilitate the distributed construction of poly-annulus conformal mapping, we establish the existence of a partition operator \mathcal{P} to reduce the topological complexity of S .

Definition III.1 (Partition Operator Admissibility). *A partition operator \mathcal{P} that decomposes S into M disjoint subdomains $\{S_k\}_{k=1}^M$ ($M \geq n$) is said to be admissible if every S_k is homeomorphic to either a unit disk \mathbb{D} or a unit annulus \mathbb{A} .*

Based on the Triangulation Theorem and topological surgery [15], S can be segmented into a finite set of simply connected patches and annular patches. This ensures the existence of an admissible operator \mathcal{P} . With existence established, the Geodesic Voronoi Tessellation (GVT) provides a feasible realization of \mathcal{P} by designing the generator set \mathcal{V} . We define a generator set $\mathcal{V} = \{v_1, \dots, v_M\} \subset S$. For a star-shaped obstacle O_k , we assign a single generator v_k in its vicinity to induce an annular cell. For a non-star-shaped obstacle O_j , a cluster $\mathcal{V}_j \subset \mathcal{V}$ ($|\mathcal{V}_j| \geq 2$) is distributed around O_j to partition its surrounding area into multiple simply connected cells. By strictly adhering to the generator design, each subdomain S_k is either Type I (Simply Connected) or Type II (Annulus containing exactly one obstacle O_k).

B. Local Partial Welding

For a non-star-shaped obstacle O_k associated with multiple generators \mathcal{V}_k , GVT segments S_k into multiple simply connected patches $\{S_{k,l}\}_{l=1}^L$, where $L = |\mathcal{V}_k| \geq 2$ denotes the number of generators assigned to O_k . It collectively encloses O_k . For notational simplicity, the subscript k is omitted. Let $S_u, S_v \in \{S_{k,l}\}_{l=1}^L$ be two adjacent patches sharing a common interface $\gamma_{uv} = \partial S_u \cap \partial S_v$. And let $h_u : S_u \rightarrow \mathbb{D}$ and $h_v : S_v \rightarrow \mathbb{D}$ be their respective Riemann mappings to the unit disk \mathbb{D} [27]. Since h_u and h_v are computed independently, the images of the common interface, $h_u(\gamma_{uv})$ and $h_v(\gamma_{uv})$ do not inherently coincide on the unit circle $\partial\mathbb{D}$. To seamlessly stitch the domain \mathbb{D}_v to \mathbb{D}_u , we seek an optimal Möbius transformation $\Theta_{uv}^* \in \text{Aut}(\mathbb{D})$ that aligns the boundary values by minimizing the welding energy functional [25]

$$\Theta_{uv}^* = \arg \min_{\Theta \in \text{Aut}(\mathbb{D})} \int_{\gamma_{uv}} |h_u(p) - \Theta(h_v(p))|^2 ds(p), \quad (8)$$

where

$$\text{Aut}(\mathbb{D}) = \left\{ z \mapsto e^{i\phi} \frac{z-a}{1-\bar{a}z} \mid \phi \in [0, 2\pi), a \in \mathbb{D} \right\}$$

denotes the group of disk automorphisms, and $ds(p)$ represents the arc length element along the interface curve γ_{uv} . By propagating Θ_{uv}^* along the boundary values across all patches, we define the composite mapping $\Theta_{1 \rightarrow l}^* = \Theta_{1,2}^* \circ \dots \circ \Theta_{l-1,l}^*$ and a piecewise unified mapping $U : \bigcup_{l=1}^L S_l \rightarrow \vartheta_k$. For any point p belonging to S_l , the map is explicitly given by

$$U(p) = \begin{cases} h_1(p), & l = 1, \\ \Theta_{1,2}^* \circ h_2(p), & l = 2, \\ \Theta_{1 \rightarrow l}^* \circ h_l(p), & l > 2. \end{cases}$$

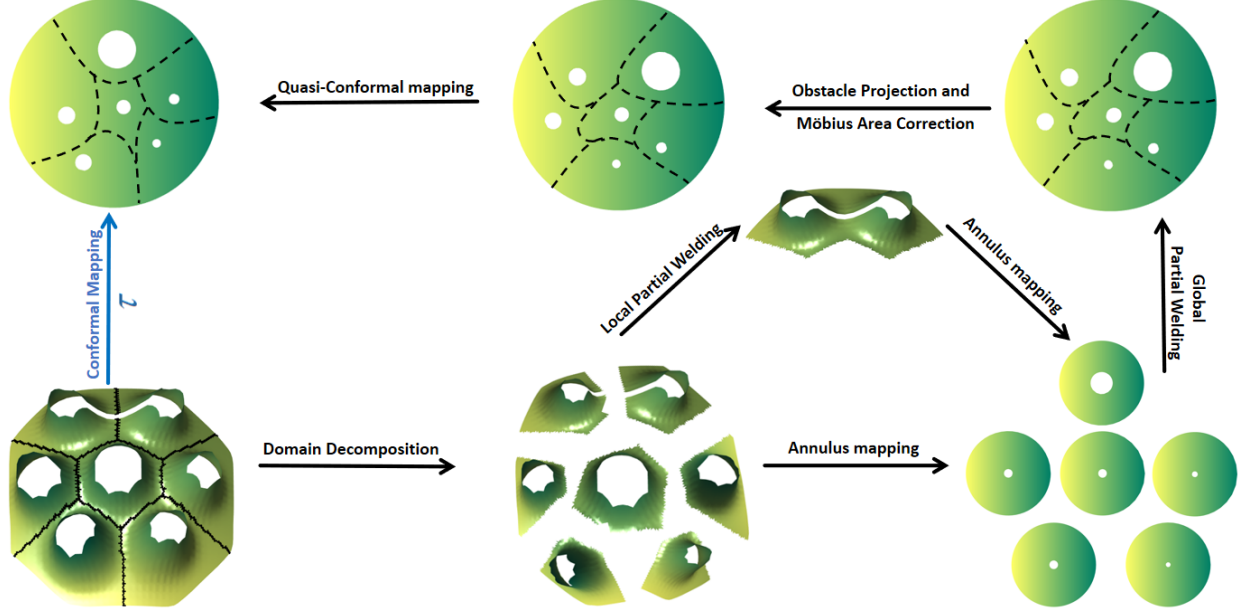


Fig. 2. The workflow of Algorithm 1. The process decomposes the complex topology into local sub-problems, stitches them via partial and global welding, and applies geometric rectification to generate a global coordinate system for the n -holed disk Ξ .

Since the union of patches $\{S_{k,l}\}_{l=1}^L$ surrounds the hole O_k , the resulting image ϑ_k is a topological annulus. An example is provided in Appendix A.

C. Parallel Annulus Mapping

This step is applicable to both the Type II subdomains and the topological annulus ϑ_k derived in Section III-B. Let ϖ_k denote the topological annulus enclosing the k -th obstacle O_k , which is defined as

$$\varpi_k = \begin{cases} S_k, & \text{if } O_k \text{ is in a Type II subregion,} \\ \vartheta_k, & \text{if } O_k \text{ is surrounded by welded patches.} \end{cases}$$

By leveraging the annulus conformal map algorithm in [23], we compute a conformal map $f_k : \varpi_k \rightarrow \mathbb{A}_k$ that transforms ϖ_k onto a circular annulus

$$\mathbb{A}_k = \{z \in \mathbb{C} \mid r_k < \|z\| < 1\}, \quad (9)$$

where $r_k \in (0, 1)$ is the conformal modulus of ϖ_k , which is uniquely determined by the domain's geometry.

Remark III.1. Due to the domain decomposition established by \mathcal{P} , the global topological complexity is decoupled into n independent annular sub-problems. Consequently, for MAS, the computation of f_k and r_k for each obstacle O_k are performed in parallel, which allows agents to solve local mappings without global information.

D. Global Partial Welding

After the parallel computation in Section III-C, we obtain a set of n disjoint annuli $\{\mathbb{A}_1, \dots, \mathbb{A}_n\}$. To assemble these local annuli while preserving the conformal structure, we introduce the partial welding operator T_k for the k -th annulus. Since the relative position and orientation of the holes must be adjusted

without distorting their local shapes, T_k is restricted to be a similarity transformation $T_k(z) = \alpha_k z + \gamma_k$, $\alpha_k \in \mathbb{C} \setminus \{0\}$, $\gamma_k \in \mathbb{C}$, where α_k controls the rotation and scaling, and γ_k determines the translation of the k -th annulus in the complex plane. Let $\iota_{ij} = \partial\varpi_i \cap \partial\varpi_j$ denote the shared interface between adjacent regions ϖ_i and ϖ_j . The optimal configuration is determined by minimizing the global stitching error

$$E_g = \sum_{(i,j) \in \mathcal{E}} \int_{\iota_{ij}} |T_i(f_i(p)) - T_j(f_j(p))|^2 ds(p), \quad (10)$$

where \mathcal{E} represents the set of adjacency indices, and $ds(p)$ denotes the arc length element along ι_{ij} . To eliminate global ambiguity, we set $T_1(z) = z$ as the reference frame ($\alpha_1 = 1$, $\gamma_1 = 0$). The minimization of (10) is a linear least-squares problem with respect to the parameters $\{\alpha_k, \gamma_k\}_{k=2}^n$, which can be solved efficiently [25]. Solving this linear system yields the optimal parameters $\{\alpha_k^*, \gamma_k^*\}_{k=1}^n$ and the corresponding global welding $g_k : \varpi_k \rightarrow \mathbb{C}$:

$$g_k(p) = T_k^*(f_k(p)), \quad \forall p \in \varpi_k. \quad (11)$$

This optimization glues the discrete annuli $\{\mathbb{A}_1, \dots, \mathbb{A}_n\}$ into a coherent domain $\Xi = \bigcup_{k=1}^n T_k^*(\mathbb{A}_k)$.

E. Geometric Rectification

The global partial welding constructed in Section III-D provides a set of piecewise mappings $\{g_k\}_{k=1}^n$. Although g_k ensures topological invariance, discrete stitching errors and conformal distortions may persist. To generate a high-quality conformal mapping $\tau : S \rightarrow \Xi$, we execute a three-stage geometric rectification process. First, we strictly enforce the circularity of the inner boundaries by computing the canonical circle (with center c_k and radius r_k) for $g_k(\partial O_k)$. The

boundary mapping \hbar_k is defined by projecting the boundary points onto these canonical circles as follows:

$$\hbar_k(p) = c_k + r_k \frac{g_k(p) - c_k}{|g_k(p) - c_k|}, \quad \forall p \in \partial O_k. \quad (12)$$

Second, to mitigate non-uniform area distortion, a global Möbius transformation $M(z, \varsigma) = \frac{z-\varsigma}{1-\bar{\varsigma}z}$ with $\varsigma \in \mathbb{D}$ is applied. We optimize the parameter ς to minimize the variance of the conformal factor $\lambda(z)$, thereby inflating the regions

$$\varsigma^* = \arg \min_{\varsigma \in \mathbb{D}} \int_{\bigcup_{g_k(\varpi_k)}} (\det(J_{M \circ \hbar}) - \bar{\lambda})^2 dA(z), \quad (13)$$

where $\det(J_{M \circ \hbar})$ represents the area distortion factor, and $\bar{\lambda}$ is the mean conformal factor. We denote $\ell = M^* \circ \hbar$ with $M^* = M(z, \varsigma^*)$. The preceding geometric rectifications inevitably introduce local angular distortions. To minimize angle distortions while maintaining the rectified circular boundaries, we solve the Laplace equation with Dirichlet boundary conditions determined by ℓ . Using the Linear Beltrami Solver (LBS) [26], the conformal mapping τ is computed by

$$\begin{cases} \Delta\tau = 0, & \text{in } S, \\ \tau(p) = \ell(p), & \text{on } \partial S. \end{cases} \quad (14)$$

This yields the diffeomorphism τ that maps the poly-annulus S to the n -holed disk Ξ . Then, we propose the Distributed Poly-Annulus Mapping Algorithm (i.e., Algorithm 1), as illustrated in Fig. 2. Finally, we prove that virtual center is computable in a distributed manner, and establish the topological conjugacy between the dynamical systems on S and Ξ .

Proposition III.1. *The following claims hold for the conformal mapping $\tau : S \rightarrow \Xi$ constructed in Algorithm 1.*

- 1) *The virtual center \mathbf{c}^* is synchronized such that $\lim_{t \rightarrow D_{\mathcal{G}}} \hat{c}_j(t) = \mathbf{c}^*, \forall j \in \mathcal{N}$.*
- 2) *The stability of dynamics on S is equivalent to that on Ξ , preserved by the scalar invariance $\dot{\mathcal{W}}(x) = \dot{\mathcal{V}}(\hat{\xi})$.*

Proof. For Claim 1), let $\partial\Xi_{out}$ be the unit circle boundary in Ξ . For agents in $\mathcal{N}_A = \{i \in \mathcal{N} \mid \partial\tau(S_i) \cap \partial\Xi_{out} \neq \emptyset\}$, they identify \mathbf{c}^* by measuring the constant curvature $\kappa_{out} = 1$ of their boundary arcs. For agents in $\mathcal{N}_I = \mathcal{N} \setminus \mathcal{N}_A$, the leader-following consensus protocol $\hat{c}_j(t+1) = (\deg_j + 1)^{-1}(\hat{c}_j(t) + \sum_{l \in \mathcal{N}_j} \hat{c}_l(t))$ ensures \mathbf{c}^* propagates across the connected graph \mathcal{G} within finite steps $D_{\mathcal{G}}$, where \deg_j denotes the node degree. For Claim 2), Since τ is a diffeomorphism on the compact manifold S , the pull-back dynamics satisfy $\dot{x} = J_{\tau}^{-1}\dot{\xi}$. The time derivative of the induced Lyapunov function $\mathcal{W}(x) = \mathcal{V}(\tau(x))$ is derived as $\dot{\mathcal{W}}(x) = (\nabla_{\hat{\xi}}\mathcal{V})^T J_{\tau} \cdot \dot{x} = (\nabla_{\hat{\xi}}\mathcal{V})^T \dot{\xi} = \dot{\mathcal{V}}(\hat{\xi})$. As $\mathcal{V}(\hat{\xi})$ ensures asymptotic stability in Ξ ($\dot{\mathcal{V}} < 0$), it directly implies $\dot{\mathcal{W}}(x) < 0$ in S . \square

Proposition III.1 provides the theoretical justification for control design in the ball world Ξ . The scalar invariance of the Lyapunov function ($\mathcal{W}(x) \equiv \mathcal{V}(\xi)$) ensures that the gradient flows in both regions are topologically conjugate. Consequently, complex collision avoidance and coverage tasks in poly-annulus S are rigorously reduced to simplified problems suitable for sectorial partition in the n -holed disk Ξ .

Algorithm 1 Distributed Poly-Annulus Mapping Algorithm

Initialize: Poly-annulus S , obstacle set \mathcal{O} , generator set \mathcal{V} .

- 1: Partition S into subdomains $\{S_k\}_{k=1}^M$ via GVT
- 2: **for** $k = 1 : M$ **do**
- 3: **if** $O_k \subset S_k$ (Type II) **then**
- 4: Set topological annulus $\varpi_k \leftarrow S_k$
- 5: **else**
- 6: Construct $\varpi_k = \vartheta_k$ via local optimal welding Θ^*
- 7: **end if**
- 8: Compute local map $f_k : \varpi_k \rightarrow \mathbb{A}_k$ via (9)
- 9: **end for**
- 10: Minimize E_g to obtain $\{\alpha_k, \beta_k\}_{k=2}^n$ via (10)
- 11: Construct global welding $\{g_k = T_k \circ f_k\}_{k=1}^n$
- 12: Update boundary $\ell = M^* \circ \hbar$ via Möbius parameter ς^*
- 13: Solve $\Delta\tau = 0$ in S with $\tau|_{\partial S} = \ell$ via (14)

Finalize: Global Conformal Mapping $\tau : S \rightarrow \Xi$.

IV. THEORETICAL RESULTS

Based on the designed conformal mapping, this section establishes the diffeomorphic coverage control framework. We first propose a multi-hole partition algorithm that modifies the partition boundaries to ensure topological safety in the ball world. Subsequently, a length metric is introduced to design a distributed control law. Theoretical analysis on the existence of solutions and the stability of partition dynamics and agent kinematics is conducted.

A. Partition Dynamics

This section proposes a distributed partition strategy in n -holed disk Ξ (the ball world) based on (5). To adapt the sectorial partition to n -holed disk Ξ , the partition bars must be modified to ensure collision avoidance while maintaining the topological connectivity of subregions. To analyze the impact of workload errors, we adopt the perturbation analysis against non-vanishing perturbations [30]. We distinguish between two geometric configurations: the linear partition bar $\hat{B}_i(\hat{\psi}_i)$ and the piecewise smooth curve $\hat{\Gamma}_i(\hat{\psi}_i)$ generated to bypass obstacles. This distinction allows us to model the actual dynamics of the workload \hat{m}_i as the nominal dynamics (governed by \hat{B}_i) superimposed with a geometric disturbance term $\hat{\delta}_i$ arising from obstacle avoidance (i.e., $\dot{m}_{i,act} = \dot{m}_{i,nom} + \hat{\delta}_i$).

We propose the Multi-Hole Partition Algorithm (i.e., Algorithm 2) to transform \hat{B}_i into $\hat{\Gamma}_i$ in a distributed manner. For every obstacle \hat{O}_k intersected by the nominal bar \hat{B}_i , we define a buffer circle $\hat{C}_{k,i}$ with radius $\hat{r}_{k,i} = \hat{r}_k(1+i\beta)$. The parameter β serves as a topological sequence factor, ensuring that the partition bars of different agents ($i \neq j$) are spatially separated when bypassing the same obstacle, thereby strictly preventing topological entanglements. The segment of partition bar inside the buffer circle $\hat{C}_{k,i}$ is replaced by a circular arc $\hat{A}_{k,i}$. (The computational details in Appendix B). The final curve $\hat{\Gamma}_i$ is constructed by concatenating these arcs $\hat{A}_i = \{\hat{A}_{k,i}\}_{k \in \hat{\mathcal{K}}_i}$ with the remaining linear segments $\hat{D}_i = [0, R] \setminus \bigcup_{k \in \hat{\mathcal{K}}_i} (\hat{p}_{in}^k, \hat{p}_{out}^k)$, where $\hat{\mathcal{K}}_i$ is the set of obstacles indices intersected by \hat{B}_i . These geometric modifications isolate partition bars from

obstacles while strictly preserving the multi-agent topological order.

Proposition IV.1. *Algorithm 2 guarantees strict collision avoidance and topological invariance within Ξ . For any agents $i, j \in \{1, \dots, N\}$ ($i \neq j$) and any obstacle \hat{O}_k , the partition bars Γ satisfy: $\hat{\Gamma}_i \cap \hat{O}_k = \emptyset$ and $\hat{\Gamma}_i \cap \hat{\Gamma}_j = \emptyset$.*

Proof. Algorithm 2 constructs the partition boundary $\hat{\Gamma}_i$ near obstacle \hat{O}_k as a circular arc with radius $\hat{r}_{k,i} = \hat{r}_k(1 + i\beta)$. Since $i \geq 1$ and $\beta > 0$, the safety radius satisfies $\hat{r}_{k,i} > \hat{r}_k$. Thus, the bar is strictly separated from the obstacle boundary $\partial\hat{O}_k$ (where radius is \hat{r}_k), ensuring $\hat{\Gamma}_i \cap \hat{O}_k = \emptyset$. To prove $\hat{\Gamma}_i \cap \hat{\Gamma}_j = \emptyset$, we first demonstrate that the ordering of agent phases $\hat{\psi}_i$ is invariant under the partition dynamics (5). Let the set of sequentially ordered phases be $\mathcal{D}_{\text{order}} = \{\hat{\psi} \in [0, 2\pi]^N \mid \hat{\psi}_1 < \hat{\psi}_2 < \dots < \hat{\psi}_N\}$. Consider the angular gap between adjacent agents: $\Delta\hat{\psi}_i(t) = \hat{\psi}_{i+1}(t) - \hat{\psi}_i(t)$ (with $\hat{\psi}_{N+1} = \hat{\psi}_1 + 2\pi$). The evolution of the angular gap $\Delta\hat{\psi}_i$ follows the discrete Laplacian flow $d\Delta\hat{\psi}_i/dt = \dot{\hat{\psi}}_{i+1} - \dot{\hat{\psi}}_i = k_{\hat{\psi}}(\hat{m}_{i+1} - 2\hat{m}_i + \hat{m}_{i-1})$. By the continuity of the density $\hat{\rho}$ on the compact manifold S , the workload \hat{m}_i vanishes as the sectorial area $\hat{E}_i \rightarrow 0$ (i.e., $\Delta\hat{\psi}_i \rightarrow 0^+$). Given the total workload $\sum_{i=1}^N \hat{m}_i > 0$, a potential singularity where $\hat{m}_i = 0$ implies that its adjacent neighbors must retain non-vanishing workloads, (i.e., $\hat{m}_{i-1} + \hat{m}_{i+1} > 0$). Consequently, the boundary velocity of the gap satisfies

$$\lim_{\Delta\hat{\psi}_i \rightarrow 0^+} \Delta\dot{\hat{\psi}}_i = k_{\hat{\psi}}(\hat{m}_{i+1} + \hat{m}_{i-1}) > 0. \quad (15)$$

This strictly positive derivative ensures that $\mathcal{D}_{\text{order}}$ is a positively invariant set [30]. The vanishing subregion induces a repulsive effect that prevents phase crossing, ensuring the bars never intersect along their linear segments. Then, consider two distinct agents i and j bypassing a same obstacle \hat{O}_k . Their spatial separation is determined by the difference in safety radii: $|\hat{r}_{k,i} - \hat{r}_{k,j}| = \hat{r}_k\beta|i - j|$. Since $i \neq j$ implies $|i - j| \geq 1$, the radial clearance is lower-bounded by $\hat{r}_k\beta > 0$. This ensures that even if two partition bars share the same angular interval during bypass, they remain disjoint in the radial dimension. Combining these two properties, we conclude $\hat{\Gamma}_i \cap \hat{\Gamma}_j = \emptyset$ for all $t \geq 0$, preserving the multi-agent topological order. \square

With the strict topological safety and ordering invariance established, the modified partition bar $\hat{\Gamma}_i$ is proven to be geometrically valid within Ξ . However, the introduction of buffer arcs inevitably causes a deviation between $\hat{\Gamma}_i$ and \hat{B}_i . The following lemma quantifies the workload error $\hat{\delta}_i$ induced by this geometric regularization.

Lemma IV.1. *The workload error $\Delta\hat{m}_i$ for the i -th agent in Algorithm 2 is strictly bounded and controllable via the parameter β .*

Proof. In Algorithm 2, when a partition bar $\hat{\Gamma}_i$ intersects with the obstacle \hat{O}_k , it is rerouted along the buffer circle with

Algorithm 2 Multi-Hole Partition Algorithm

Initialize: Agent number N , obstacles \hat{O} , sequence factor β , radius of n -holed disk R .

```

1: for  $i = 1 : N$  do
2:   Update partition bar  $\hat{B}_i(\hat{\psi}_i)$  with  $\hat{\psi}_i$  via (5)
3:   Identify  $\hat{\mathcal{K}}_i = \{k \mid \hat{B}_i \cap \hat{O}_k \neq \emptyset\}$ 
4:   for each  $k \in \hat{\mathcal{K}}_i$  do
5:     Set  $\hat{\mathcal{C}}_{k,i}$  with  $\hat{r}_{k,i} = \hat{r}_k(1 + i\beta)$ 
6:     Construct arc  $\hat{A}_{k,i} \subset \hat{\mathcal{C}}_{k,i}$  s.t.  $\partial\hat{A}_{k,i} = \hat{B}_i \cap \hat{\mathcal{C}}_{k,i}$ .
7:   end for
8:    $\hat{\Gamma}_i = ([0, R] \setminus \bigcup_{k \in \hat{\mathcal{K}}_i} (\hat{p}_{in}^k, \hat{p}_{out}^k)) \bigoplus_{k \in \hat{\mathcal{K}}_i} \hat{A}_{k,i}$ .
9: end for

```

Finalize: Modified partition bars $\hat{\Gamma} = \{\hat{\Gamma}_1, \dots, \hat{\Gamma}_N\}$.

radius $\hat{r}_{k,i} = \hat{r}_k(1 + i\beta)$. The workload error contributed by \hat{O}_k is given by

$$\Delta\hat{m}_{k,i} = \int_{\hat{\theta}_{s,k}}^{\hat{\theta}_{e,k}} \int_{\hat{r}_k}^{\hat{r}_{k,i}} \hat{\rho}(\hat{r}, \hat{\theta}) \hat{r} d\hat{r} d\hat{\theta},$$

where $\Delta\hat{\theta}_k = \hat{\theta}_{e,k} - \hat{\theta}_{s,k}$ is the angular span. Since the density $\hat{\rho}$ is continuous on the compact set S , it is bounded by $\|\hat{\rho}\|_\infty$. Evaluating the inner radial integral yields $\int_{\hat{r}_k}^{\hat{r}_{k,i}} \hat{r} d\hat{r} = \hat{r}_k^2 i\beta + \frac{1}{2} \hat{r}_k^2 i^2 \beta^2$. For a small sequence factor $\beta \ll 1$, the second-order term β^2 is negligible. Summing over all obstacles $k \in \hat{\mathcal{K}}_i$ intersected by $\hat{\Gamma}_i$, and considering the worst-case agent index $i = N$, the total workload error satisfies

$$\Delta\hat{m}_i = \sum_{k \in \hat{\mathcal{K}}_i} \Delta\hat{m}_{k,i} \leq \beta \cdot N \cdot C_g \cdot \|\hat{\rho}\|_\infty, \quad (16)$$

where $C_g = \sum_{k=1}^n L_k \hat{r}_k$ is a positive constant and $L_k = \hat{r}_k \Delta\hat{\theta}_k$. By defining $C_{\hat{\delta}} = N C_g \|\hat{\rho}\|_\infty$, we obtain $\Delta\hat{m}_i \leq C_{\hat{\delta}} \beta$. Thus, the workload deviation $\Delta\hat{m}_i$ is controllable via β and vanishes as $\beta \rightarrow 0$. \square

While the partition dynamics can ensure the topological safety of the virtual bars $\hat{\Gamma}_i$, a robust motion planning strategy is required for agents to navigate in their corresponding sub-regions \hat{E}_i . Note that Euclidean control laws may fail to prevent collisions with the intricate boundaries of the poly-annulus surface S . To address this, the following subsection constructs a safety-aware Riemannian metric to govern the agent kinematics.

B. Design of Distributed Controller

This section establishes a geometric coordination mechanism for agent navigation on the poly-annulus S . First, a Riemannian length metric is constructed to encode obstacles avoidance. Second, a Riemannian gradient-based control law is synthesized as a flow on the resulting manifold to ensure autonomous navigation.

1) *Design of Length Metric:* In the mapping space Ξ , let $\hat{p} = (\hat{r}, \hat{\theta})$ be the coordinate in a local chart. The distance from \hat{p} to the boundary of the k -th obstacle \hat{O}_k (centered at \hat{o}_k) is $\hat{s}_k(\hat{p}) = \|\hat{p} - \hat{o}_k\| - \hat{r}_k$. To ensure the validity and smoothness of the navigation space, we construct a static weight function

$\hat{\sigma}_0(\hat{p}) = \sum_{k=1}^n (e^{\mu\hat{s}_k(\hat{p})} - 1)^{-1}$, where $\mu > 0$ is a curvature parameter. As $\hat{s}_k \rightarrow 0^+$, the weight $\hat{\sigma}_0 \rightarrow \infty$, which characterizes the infinite navigation cost at the boundaries. The Riemannian metric $\hat{\eta}_0$ on Ξ is defined as

$$\hat{\eta}_0(\hat{p}) = (1 + \hat{\sigma}_0(\hat{p}))^2 \text{diag}(1, \hat{r}^2). \quad (17)$$

This metric is pulled back to the poly-annulus S as $\eta_0(p) = \lambda^2(p)\hat{\eta}_0(\tau(p))$, where $\lambda(p) = \sqrt{|\det(J_\tau(p))|}$ is the conformal factor induced by the Jacobian $J_\tau = \partial\tau/\partial p$. The associated length metric $d_l(p, q)$ is defined as the infimum of path lengths:

$$d_l(p, q) = \inf_{\gamma} \left\{ \int_0^1 \sqrt{\dot{\gamma}(t)^T \eta_0(\gamma(t)) \dot{\gamma}(t)} dt \right\}, \quad (18)$$

where γ is a piecewise smooth curve such that $\gamma(0) = p$ and $\gamma(1) = q$. Notably, d_l is defined solely based on static obstacles to ensure a time-invariant geometric workspace for the cost function (6).

2) *Design of Control Law:* While the length metric d_l governs global navigation, inter-agent collision avoidance is integrated via a dynamic metric. Let $\Omega_{ij} = \{p_i \in S \mid \|p_i - p_j\| \leq 2r_a\}$ denote the inter-agent collision set with agent radius r_a . Then define the feasible set $\mathcal{F}_i = S \setminus (\bigcup_{k=1}^n O_k \cup \bigcup_{j \in \mathcal{N}_i} \Omega_{ij})$. For the i -th agent, the composite weight is $\hat{\sigma}_i = \hat{\sigma}_0 + \sum_{j \in \mathcal{N}_i} \hat{\sigma}_{ij}$, where $\hat{\sigma}_{ij} = (e^{\mu(\|\hat{p}_i - \hat{p}_j\| - 2r_a)} - 1)^{-1}$ accounts for the proximity to neighbor j . Let $\hat{\eta}_i = (1 + \hat{\sigma}_i)^2 \text{diag}(1, \hat{r}^2)$ be the local Riemannian metric in Ξ . To ensure the well-posedness of the induced dynamic manifold, we impose the following regularity condition.

Assumption IV.1 (Safety Clearance). *There exists a constant $\delta > 0$ such that the neighbor trajectories satisfy separation: $\hat{d}_{ij} \geq 2r_a + \delta$, $\forall t \geq 0$, $\forall j \in \mathcal{N}_i$, where $\hat{d}_{ij} = d_l(\hat{p}_i, \hat{p}_j)$. This condition restricts the system configuration to a compact subset of the feasible set \mathcal{F}_i , preventing metric singularities.*

Based on this safety clearance assumption, the evolution of the Riemannian metric is mathematically bounded. Then, to ensure the effectiveness of the control input design, we need to analyze the relationship between the control input and the variation rate of the Riemannian metric.

Lemma IV.2. *Under Assumption IV.1, the time derivative of the pull-back metric $\eta_i(t)$ satisfies $\|\dot{\eta}_i\|_F \leq L_\eta \sum_{j \in \mathcal{N}_i} \|\dot{\hat{p}}_j\|$, where $L_\eta > 0$. Consequently, it asymptotically recovers a static manifold.*

Proof. Applying the chain rule to $\eta_i = \lambda^2(1 + \hat{\sigma}_i)^2 \text{diag}(1, \hat{r}^2)$ leads to $\dot{\eta}_i = 2\lambda^2(1 + \hat{\sigma}_i) \text{diag}(1, \hat{r}^2) \sum_{j \in \mathcal{N}_i} (\partial \hat{\sigma}_{ij} / \partial \hat{d}_{ij}) \cdot (d\|\hat{p}_i - \hat{p}_j\|/dt)$. On the compact set \mathcal{F}_i , the terms $2\lambda^2(1 + \hat{\sigma}_i)$ and $\text{diag}(1, \hat{r}^2)$ are bounded. By Assumption IV.1, the condition $\hat{d}_{ij} \geq 2r_a + \delta$ ensures a uniform upper bound

$$\begin{aligned} \|\partial \hat{\sigma}_{ij} / \partial \hat{d}_{ij}\| &= \| -\mu e^{\mu(\hat{d}_{ij} - 2r_a)} (e^{\mu(\hat{d}_{ij} - 2r_a)} - 1)^{-2} \| \\ &\leq \mu e^{\mu\delta} (e^{\mu\delta} - 1)^{-2} < \infty. \end{aligned}$$

Since $|d\|\hat{p}_i - \hat{p}_j\|/dt| \leq \|\dot{\hat{p}}_i\| + \|\dot{\hat{p}}_j\|$, there exists a constant L_η such that $\|\dot{\eta}_i\|_F \leq L_\eta \sum_{j \in \mathcal{N}_i} \|\dot{\hat{p}}_j\|$, which implies $\lim_{t \rightarrow \infty} \dot{\hat{p}}(t) = 0 \implies \lim_{t \rightarrow \infty} \dot{\eta}_i(t) = 0$. \square

In light of Lemma IV.2, the control input u_i is designed as the Riemannian gradient flow on the instantaneous manifold

$$\mathbf{u}_i = -k_p \nabla_{\eta, p_i} J = -k_p \eta_i^{-1}(p_i) \frac{\partial J}{\partial p_i}, \quad (19)$$

where $k_p > 0$ is the gain and Riemannian metric η_i is the pull-back of $\hat{\eta}_i = (1 + \hat{\sigma}_i)^2 \text{diag}(1, \hat{r}^2)$. This formulation defines u_i as a geometric invariant, where the transformation of η_i naturally compensates for coordinate changes to maintain the consistency across local charts [8].

Proposition IV.2. *The following properties hold for the control input (19) on the feasible set \mathcal{F}_i .*

- 1) *Non-degeneracy:* $\eta_i \in \mathbb{S}_{++}^2$, $\|\eta_i\| < \infty$, $\forall p_i \in \mathcal{F}_i$.
- 2) *Equivalence:* $\nabla_{\eta, p_i} J = 0 \iff \frac{\partial J}{\partial p_i} = 0$.
- 3) *Invariance:* $p_i(0) \in \mathcal{F}_i \implies p_i(t) \in \mathcal{F}_i, \forall t \geq 0$.

Proof. For Claim 1), as τ is a conformal mapping, its Jacobian J_τ is non-singular, ensuring conformal factor $\lambda^2 = |\det(J_\tau)| > 0$ on poly-annulus S . Since $\hat{\sigma}_i$ is a composition of continuous exponential functions and is finite on the compact set \mathcal{F}_i . Thus, the scalar scaling $\lambda^2(1 + \hat{\sigma}_i)^2$ is strictly positive and bounded, ensuring $\eta_i \in \mathbb{S}_{++}^2$ (2×2 symmetric positive definite) and its induced matrix norm $\|\eta_i\|$ is finite $\forall p_i \in \mathcal{F}_i$. For Claim 2), η_i is non-degenerate according to Claim 1). The Riemannian gradient $\nabla_{\eta, p_i} J = \eta_i^{-1} \frac{\partial J}{\partial p_i}$ is the image of the differential dJ under the isomorphism $T^*S \rightarrow TS$. Since η_i^{-1} is an invertible linear operator, its kernel is trivial, ensuring the equivalence of the critical points. For Claim 3), as p_i approaches the boundary $\partial\mathcal{F}_i$, the divergence $\hat{\sigma}_i \rightarrow \infty$ ensures that η_i^{-1} vanishes. The asymptotic behavior is governed by $\lim_{p_i \rightarrow \partial\mathcal{F}_i} \eta_i^{-1} = \lim_{\hat{\sigma}_i \rightarrow \infty} (1 + \hat{\sigma}_i)^{-2} \text{diag}(1, \hat{r}^{-2})/\lambda^2 = 0$. The vanishing of the inverse metric η_i^{-1} at $\partial\mathcal{F}_i$ nullifies the normal component of u_i . Following Nagumo's Theorem [30], the trajectory is confined to \mathcal{F}_i for all $t \geq 0$. \square

Given the continuous-time dynamics (5) and (19), we need to address their distributed implementation. The following subsection introduces a numerical scheme that projects Riemannian gradient flows onto a discrete-time execution framework.

C. Poriferous Coverage Algorithm

To approximate the optimal solution to the constrained optimization problem (7), we develop the Poriferous Coverage Optimization Algorithm (i.e., Algorithm 3). This algorithm bridges the continuous geometric theory with a distributed computational implementation. Initially, a quantization parameter ε_p is defined to discretize the partition process into $K^* = \lceil 2\pi/\varepsilon_p \rceil$ intervals. For each $k \in \{1, \dots, K^*\}$, the index set $\chi_k = \{i \in \mathbb{I}_N \mid i = \arg \min_j |\hat{\psi}_j - 2\pi(k-1)/K^*|\}$ identifies the anchor agent closest to the reference phase. During the execution horizon $t < T_\epsilon$, the dynamics are updated based on agent roles. For the anchor agent $a \in \chi_k$: The partition phase is fixed as $\hat{\psi}_a = 2\pi(k-1)/K^*$ to serve as a spatial reference. Its mapped position \hat{p}_a and physical position p_a evolve according to the corresponding Riemannian gradient (19). For all other agents $i \notin \chi_k$: The partition phases $\hat{\psi}_i$ are updated via the dynamics (5). Simultaneously, their positions are synchronized across S and Ξ through the pull-back length

Algorithm 3 Poriferous Coverage Optimization Algorithm**Initialize:** \mathcal{N} , τ , K^* , T_ϵ , and $J^* \leftarrow \infty$.

```

1: for  $k = 1$  to  $K^*$  do
2:   Set  $\hat{\psi}_k \leftarrow 2\pi(k-1)/K^*$ 
3:   Set  $a \leftarrow \arg \min_{j \in \mathcal{N}} |\hat{\psi}_j - \hat{\psi}_k|$ 
4:   while  $t < T_\epsilon$  do
5:     for each agent  $i \in \mathcal{N}$  do
6:        $\hat{\psi}_i \leftarrow \hat{\psi}_k$  if  $i = a$ , else evolve  $\hat{\psi}_i$  via (5)
7:       Construct  $\hat{\Gamma}_i$  in  $\Xi$  and compute  $u_i$  via (19)
8:       Update  $p_i$  via (3) and synchronize  $\dot{p}_i = \tau(p_i)$ 
9:     end for
10:     $t \leftarrow t + \Delta t$ 
11:  end while
12:  Update  $(J^*, \hat{\psi}^*, p^*) \leftarrow (J, \hat{\psi}, p)$  via (6) if  $J < J^*$ 
13: end for
Finalize: Optimal configuration  $(\hat{\psi}^*, p^*)$ 

```

metric (18) and the conformal mapping τ . Furthermore, the global cost J^k for each discrete initialization is evaluated via a distributed communication mechanism [12]. Finally, the system selects $k^* = \arg \min_k J^k$ to finalize the optimal configuration $(\hat{\psi}^*, p^*)$. Algorithm 3 relies on the rigorous interplay between virtual partition bars and multi-agent motion. To certify the reliability, we provide a theoretical analysis on the existence of solutions, the input-to-state stability (ISS) of partition dynamics, and the asymptotic convergence of the closed-loop system.

D. Convergence Analyses

This subsection focuses on the convergence of the proposed coverage control algorithm. At first, we analyze the existence of solutions to Problem (7).

Proposition IV.3. *There always exist optimal solutions to Problem (7) in poly-annulus S , and these solutions are reachable for multi-agent dynamics (3) with control input (19).*

Proof. The surface S is a compact 2D Riemannian manifold with a smooth boundary, which implies the joint configuration space $\mathcal{Q} = S^N \times [0, 2\pi]^N$ is compact because it is the Cartesian product of compact sets. The cost functional J in (6) is defined via the length metric d_l , which is induced by the continuous and positive definite pull-back metric η_i . Consequently, J is a continuous functional on the compact set \mathcal{Q} . By the *Weierstrass Extreme Value Theorem* [32], J must attain its global minimum, which confirms the existence of the optimal configuration $(\hat{\psi}^*, p^*)$. For the global reachability, by the properties of cut loci on Riemannian manifolds [29], the distance function d_l is smooth almost everywhere, ensuring that the Riemannian gradient $\nabla_{\eta} J$ is well-defined. In addition, since (S, η_i) is a compact manifold, it is geodesically complete according to the *Hopf-Rinow Theorem* [27]. Furthermore, the metric singularity $\hat{\sigma}_i \rightarrow \infty$ at the boundary $\partial \mathcal{F}_i$ induces a repelling potential that renders the interior of the feasible set forward invariant [30]. Thus, the system trajectories $\mathbf{p}(t)$ globally exist for all $t \in [0, \infty)$. Finally, consider the coverage

cost J as a Lyapunov candidate. Its time derivative along the system trajectories is given by:

$$\frac{dJ}{dt} = \sum_{i=1}^N \langle \nabla_{\eta_i} J, \dot{p}_i \rangle \eta_i = -k_p \sum_{i=1}^N |\nabla_{\eta_i} J| \eta_i^2 \leq 0. \quad (20)$$

By *LaSalle's Invariance Principle* [30], since trajectories are bounded and $\dot{J} \leq 0$, the state asymptotically converges to the largest invariant set $\{(\hat{\psi}, \mathbf{p}) \mid \nabla \eta J = 0\}$. Given that local minima are stable equilibria of the gradient flow, the system converges to the optimal coverage configuration. \square

While Proposition IV.3 ensures the existence of optimal configurations on (S, η_i) , the trajectories of physical system are governed by the coupled dynamics of $\hat{\psi}_i$ and \dot{p}_i . A significant challenge arises from the geometric regularization in Algorithm 2, which introduces a non-vanishing perturbation $\hat{\delta}(t)$ to the partition dynamics. To solve this problem, the following theorem establishes the robustness of partition dynamics against this modification.

Theorem IV.1. *The workload error is exponentially input-to-state stable with respect to the sequence factor β , satisfying $\|\mathbf{e}(t)\| \leq \|\mathbf{e}(0)\| e^{-\gamma t} + C_{\hat{\delta}} \beta / \gamma$, where $\mathbf{e}(t) = \mathbf{m}(t) - \bar{\mathbf{m}} \cdot \mathbf{1}_N$ with $\mathbf{m}(t) = (m_1(t), \dots, m_N(t))^T$, and γ is the exponential convergence rate. Consequently, the ultimate error bound can be made arbitrarily small by refining β .*

Proof. Construct the Lyapunov function as $V = \frac{1}{2} \|\mathbf{e}\|^2$. For the connected cycle graph $\mathcal{G}_N = (\mathcal{N}, \mathcal{E})$, the error dynamics obey $\dot{\mathbf{e}} = -k_{\hat{\psi}} \mathcal{L}_{\mathcal{G}}(\hat{\omega}) \mathbf{e}$, where the weighted Laplacian $\mathcal{L}_{\mathcal{G}}$ is defined by

$$[\mathcal{L}_{\mathcal{G}}]_{ij} = \begin{cases} \hat{\omega}_i + \hat{\omega}_{i+1}, & i = j \\ -\hat{\omega}_{\max(i,j)}, & (i, j) \in \mathcal{E} \\ 0, & \text{otherwise} \end{cases} \quad (21)$$

The properties of $\mathcal{L}_{\mathcal{G}}$ are detailed in Appendix C. Under Assumption IV.1 ($\hat{\omega} > 0$), $\mathcal{L}_{\mathcal{G}}$ is symmetric positive semi-definite with $\ker(\mathcal{L}_{\mathcal{G}}) = \text{span}(\mathbf{1}_N)$. Since $\mathbf{e} \perp \mathbf{1}_N$, invoking the *Courant-Fischer Theorem* [31, Th. 4.2.2] yields

$$\dot{V}_{\text{nom}} = -k_{\hat{\psi}} \mathbf{e}^T \mathcal{L}_{\mathcal{G}}(\hat{\omega}) \mathbf{e} \leq -k_{\hat{\psi}} \hat{\omega} \lambda_2(\mathcal{L}_S) \|\mathbf{e}\|^2 \triangleq -\gamma \|\mathbf{e}\|^2,$$

where \mathcal{L}_S is the unweighted Laplacian of a cycle graph with algebraic connectivity $\lambda_2(\mathcal{L}_S) = 2(1 - \cos(2\pi/N))$ and $\gamma > 0$ denotes the exponential convergence rate. Algorithm 2 introduces a disturbance $\|\hat{\delta}(t)\| \leq C_{\hat{\delta}} \beta$. The actual derivative becomes $\dot{V} \leq -\gamma \|\mathbf{e}\|^2 + C_{\hat{\delta}} \beta \|\mathbf{e}\|$. Splitting the dissipation with $\theta \in (0, 1)$ gives

$$\dot{V} \leq -(1 - \theta) \gamma \|\mathbf{e}\|^2 - \theta \gamma \|\mathbf{e}\| (\|\mathbf{e}\| - C_{\hat{\delta}} \beta / \theta \gamma).$$

For $\|\mathbf{e}\| \geq C_{\hat{\delta}} \beta / \theta \gamma$, one has $\dot{V} \leq -2(1 - \theta) \gamma V$. By the *Comparison Lemma* [30, Th. 4.19], the trajectory is bounded by

$$\|\mathbf{e}(t)\| \leq \max\{\|\mathbf{e}(0)\| e^{-(1-\theta)\gamma t}, C_{\hat{\delta}} \beta / \theta \gamma\}.$$

By taking $\theta \rightarrow 1$, the error converges to $\limsup_{t \rightarrow \infty} \|\mathbf{e}(t)\| \leq C_{\hat{\delta}} \beta / \gamma$, establishing exponential ISS with a controllable ultimate bound, where the adjustability of β is rigorously guaranteed by Lemma IV.1. \square

Based on the exponential ISS established in Theorem IV.1, the workload error $e(t)$ is strictly bounded by the perturbation β . To ensure the global coverage performance, it is imperative that agent trajectories $p(t)$ in poly-annulus S accurately track the evolving optimal configurations. Thus, we establish the stability of the Riemannian gradient flow (19) to guarantee the synchronization of physical states in the robot workspace with the virtual partitions in the ball world.

Theorem IV.2. *The control law (19) asymptotically stabilizes each agent to the Riemannian centroid p_i^* of its subregion E_i in poly-annulus S . Moreover, this equilibrium is locally exponentially stable.*

Proof. Global asymptotic convergence of $p(t)$ to the critical set is established in Proposition IV.3. Under the Riemannian gradient flow $\dot{p}_i = -k_p \nabla_{\eta, p_i} J$, the time derivative satisfies $\dot{J} = -k_p \sum_{i=1}^N \|\nabla_{\eta, p_i} J\|_{\eta_i}^2 \leq 0$. The equilibrium condition $\nabla_{\eta, p_i} J = 0$ uniquely defines the set of Riemannian centroids $\{p_i^*\} \subset \mathcal{F}_i$. Crucially, the vanishing of η_i^{-1} at $\partial \mathcal{F}_i$ ensures the forward invariance of the collision-free set \mathcal{F}_i , as proved in Proposition IV.2. To establish local exponential stability, we evaluate the positivity of the Hessian operator $\nabla^2 J$ at the equilibrium. According to Lemma IV.2, the metric $\eta_i(t)$ asymptotically recovers a static manifold as partition dynamics (5) stabilizes. This justifies a quasi-static analysis of the agent dynamics. In Ξ . Under Assumption II.1, the Hessian $\nabla^2 \hat{J}_i$ for a fixed partition is given by

$$\nabla^2 \hat{J}_i(\hat{p}_i) = \int_{\hat{E}_i} (f''(d_{\hat{i}}) \nabla d_{\hat{i}} \otimes \nabla d_{\hat{i}} + f'(d_{\hat{i}}) \nabla^2 d_{\hat{i}}) \hat{\rho}(\hat{q}) d\hat{q}.$$

Since $f' > 0$, $f'' > 0$, and $\nabla^2 d_{\hat{i}} \succ 0$ within the convexity radius of Ξ , it follows $\nabla^2 \hat{J}_i(\hat{p}_i^*) \succ 0$. By the pull-back $J = \hat{J} \circ \tau$, the Hessian at p^* is transformed via the Jacobian of τ : $\nabla^2 J(p^*) = (J_\tau)^T \nabla^2 \hat{J}(\hat{p}_i^*) J_\tau$ with $J_\tau = \partial \tau / \partial p$. Since τ is a diffeomorphism, J_τ is non-singular. By *Sylvester's Law of Inertia* [27], the positive definiteness of the operator is invariant under this congruence transformation, i.e., $\nabla^2 J_S(p^*) \succ 0$. Linearizing the Riemannian flow $\dot{p}_i = -k_p \nabla_{\eta, p_i} J$ around p^* yields the system matrix $-k_p \nabla^2 J(p^*)$. Since $\nabla^2 J(p^*)$ is strictly positive definite, all eigenvalues lie in the open left-half complex plane, and p_i^* is locally exponentially stable. \square

The exponential ISS of partition dynamics (5) and the local stability of agent dynamics (3) ensure that the MAS tracks the Riemannian centroids p_i^* with high fidelity. However, in practical implementations, the global coverage performance is influenced by the discrete properties of MAS and the finite sampling frequency. Based on the convergence results in Theorem IV.1 and Theorem IV.2, we evaluate the gap between the actual cost $J(\hat{\psi}^A, p^A)$ and the theoretical optimum $J(\hat{\psi}^*, p^*)$ to establish the global quasi-optimality of the proposed algorithm.

Theorem IV.3. *Algorithm 3 steers MAS to approximate the optimal configuration and ensures the coverage cost J is minimized within an arbitrarily small tolerance.*

Proof. Let $\mathcal{X} = (\hat{\psi}, p)$ denote the joint state on the product manifold $\mathbb{T}^N \times S^N$. By the triangle inequality, the cost deviation is decomposed into three distinct terms below

$$\begin{aligned} |J(\mathcal{X}^*) - J(\mathcal{X}^A)| &\leq |J(\hat{\psi}^*, p^*) - J(\hat{\psi}^*, p^k)| \\ &\quad + |J(\hat{\psi}^*, p^k) - J(\hat{\psi}^k, p^k)| \\ &\quad + |J(\hat{\psi}^k, p^k) - J(\hat{\psi}^A, p^A)| + \epsilon_{conv}, \end{aligned} \quad (22)$$

where ϵ_{conv} represents the convergence residual due to the finite termination horizon T_ϵ . For the first term, it quantifies the discrepancy between the continuous trajectory $p(t)$ and the discrete sequence p^k , which is updated via $p_{k+1} = \exp_{p_k}(-k_p \Delta t \nabla_{\eta_i} J)$ [33]. Since the poly-annulus S is compact, the forward invariance of \mathcal{F}_i established in Proposition IV.2 coupled with the *Hopf-Rinow Theorem* [27] ensures that S is geodesically complete, rendering the discrete update globally well-defined. Applying the second-order covariant Taylor expansion, the cost variation is dominated by the Riemannian Hessian $\nabla^2 J$. Invoking Assumption II.1 ($f', f'' > 0$), the compactness of S ensures a finite Hessian upper bound $L_H = \sup_{p \in S} \|\nabla^2 J(p)\|_l$, where $\|\cdot\|_l$ denotes the operator norm induced by the length metric $d_l(\cdot)$. L_H explicitly incorporates the curvature of S and the performance supremum $\bar{f}'' = \sup f''$. Thus, one gets

$$|J(\hat{\psi}^*, p^*) - J(\hat{\psi}^*, p^k)| \leq 0.5 L_H \|\nabla_{\eta_i} J\|_{l, \max}^2 (\Delta t)^2, \quad (23)$$

where the zeroth and first-order terms cancel exactly as the discrete retraction is intrinsically aligned with the Riemannian gradient flow.

For the second term, it stems from the quantization of the configuration torus \mathbb{T}^N into K^* intervals, which induces a geodesic deviation $d_{\hat{\psi}}(\hat{\psi}^*, \hat{\psi}^k) \leq 2\pi/K^*$. Invoking Assumption II.1 ($f' > 0$), we apply the *Stokes' Theorem* [27] to the boundary $\partial \hat{E}_i$, the intrinsic gradient is $\nabla_{\hat{\psi}_i} J = (f(d_l(p_i, q)) - f(d_l(p_{i-1}, q))) \hat{\omega}(\hat{\psi}_i)$, where $\hat{\omega}(\hat{\psi}_i)$ denotes the marginal density at the i -th partition bar. Consequently, the quantization error is bounded by

$$|J(\hat{\psi}^*, p^k) - J(\hat{\psi}^k, p^k)| \leq L_{\hat{\psi}} (2\pi/K^*), \quad (24)$$

where $L_{\hat{\psi}} = \sup_{\hat{\psi}} \|\nabla_{\hat{\psi}} J\|_l$ is constrained by $\bar{f}' = \sup f'$ and the maximum total variation of the Riemannian volume form across the boundaries $\partial \hat{E}_i$ in Ξ .

For the third term, it stems from the geometric regularization β in Algorithm 3. The rerouting of partition bars from B_i to \hat{B}_i induces a domain perturbation $\Delta \mathcal{M}_i \subset S$. By invoking *Stokes' Theorem* [27], the cost deviation is

$$\begin{aligned} |J(\mathcal{X}^k) - J(\mathcal{X}^A)| &= \left| \sum_{i=1}^N \int_{\Delta \mathcal{M}_i} f(d_l(p_i, q)) \rho(q) dV_l \right| \\ &\leq L_g C_\delta \beta, \end{aligned} \quad (25)$$

where $L_g = \sup f(d_l)$ is the performance bound on S . In light of Lemma IV.1, the workload deviation $|\Delta \hat{m}_i| \leq C_\delta \beta$ linearly maps to the cost penalty via the conformal factor λ^2 of the pull-back volume form $dV_l = \det(\tau^* \hat{\eta}_0)^{1/2} dx$. As established in Theorem IV.2, $\nabla^2 J \succ 0$ at equilibrium ensures Geodesic Strong Convexity. For the performance function f satisfying Assumption II.1, the quadratic growth condition on

the manifold S [34] provides a rigorous bound on the state deviation in the length metric $d_l(\cdot)$:

$$d_l(\mathcal{X}^A, \mathcal{X}^*) \leq \sqrt{2(J(\mathcal{X}^A) - J(\mathcal{X}^*))/\lambda_{\min}(\nabla^2 J)}, \quad (26)$$

where $\lambda_{\min}(\nabla^2 J)$ is the minimum eigenvalue of the Riemannian Hessian. \square

E. Topological Universality

The preceding analyses confirm the algorithm performance on the poly-annulus surface. However, the fundamental validity of this framework transcends specific obstacle shapes. As a result, we abstract the workspace into a Riemannian manifold (\mathcal{M}, η) and establish the maximal topological class for which the proposed diffeomorphic control is strictly applicable.

Theorem IV.4. *The proposed framework is applicable to the maximal class of compact, orientable, 2-D Riemannian manifolds (\mathcal{M}, η) with boundary, satisfying the Euler characteristic $\chi(\mathcal{M}) = 1 - n$ and Genus $g(\mathcal{M}) = 0$. For any \mathcal{M} in this class, the distributed coverage problem is topologically conjugate to the harmonic gradient flow on the n -holed disk Ξ .*

Proof. The proof relies on De Rham Cohomology theory to establish the existence of the coordinate system required by partition dynamics (5) and agent model (3). First of all, we prove the cohomological existence of partition phase ψ . The validity of sectorial partition depends on a global angular coordinate $\hat{\psi}$ that uniquely indexes the topology. In terms of differential forms, this requires a non-trivial closed 1-form $\omega \in H_{dR}^1(\mathcal{M})$. For Genus-0 manifolds with $n + 1$ boundary components, $H_{dR}^1(\mathcal{M})$ is an n -dimensional vector space. By the *Hodge Decomposition Theorem* [15], there exists a unique harmonic 1-form ω_h ($\Delta\omega_h = 0$). Then, the conformal mapping $\tau : \mathcal{M} \rightarrow \Xi$ is the holomorphic integration of ω_h , where the partition phase $\hat{\psi}$ is the period integral of the pull-back form $\tau^*\hat{\omega}$. This ensures that boundaries ∂E_i are harmonic level sets, maintaining orthogonality to the Riemannian gradient flow. Then, we analyze the topological conjugacy of agent dynamics. Agent motion is governed by the vector field $X = -\nabla_\eta J$ on \mathcal{M} . The conformal diffeomorphism τ induces an isomorphism between tangent bundles $T\mathcal{M}$ and $T\Xi$. The push forward operator τ_* maps the gradient field to $X_\Xi = -\nabla_{\hat{\eta}}\hat{J}$ on Ξ via $X_\Xi = \lambda^{-2}\tau_*X$, with λ^2 being the conformal factor. By the *Poincaré-Hopf Theorem* [15], the sum of vector field indices equals $\chi(\mathcal{M})$. Since $\chi(\mathcal{M}) = \chi(\Xi) = 1 - n$, the equilibrium set (centroids) remains a topological invariant. Thus, the convergence established in Theorem IV.2 on Ξ extends to any \mathcal{M} within this class, regardless of boundary irregularity. Finally, we analyze the genus constraint. The restriction to genus $g(\mathcal{M}) = 0$ is rigorous. If $g(\mathcal{M}) > 0$, the non-commutative fundamental group $\pi_1(\mathcal{M})$ introduces handle cycles in $H_{dR}^1(\mathcal{M})$ that do not correspond to obstacles. A 1-dimensional angular ordering $\hat{\psi} \in [0, 2\pi]$ fails to characterize the state relative to these handles without complex branch cuts. Thus, $\chi(\mathcal{M}) = 1 - n$ with Genus 0 defines the upper bound for 1-dimensional sectorial coverage. \square

The theoretical analysis constitutes a rigorous chain of logical deductions, guaranteeing the system reliability across

geometric, dynamic, and computational implementation. First, Proposition IV.3 establishes the topological conjugacy and existence of the coordinate system via the conformal mapping τ , while the metric pull-back $\eta = \tau^*\hat{\eta}_0$ preserves the intrinsic geometry of the poly-annulus. Building on this, Lemma IV.1 and Proposition IV.1 confirm the strict geometric safety of sectorial partitions, ensuring that the boundaries $\hat{\Gamma}_i$ are harmonic level sets that remain valid under constraints. Regarding control feasibility, Proposition IV.2 guarantees the non-degeneracy and forward invariance of the feasible set \mathcal{F}_i , ensuring that the Riemannian gradient flow is globally well-defined and collision-free. This is further supported by Lemma IV.2, which proves the metric regularity of the pull-back manifold. This indicates that it asymptotically recovers a static structure as the agents converge. Subsequently, the stability analysis reveals a hierarchical convergence structure. To be specific, Theorem IV.1 proves that the virtual partition dynamics $\hat{\psi}$ exhibit exponential ISS against geometric perturbations β , as supported by the contraction properties in Lemma IV.1. Coordinated with the robust partitions, Theorem IV.2 guarantees that the multi-agent kinematics p asymptotically converge to the optimal Riemannian centroids with local exponential rates. Theorem IV.3 bridges the gap between continuous theory and discrete implementation by validating that the numerical outputs strictly approximate the theoretical optimum \mathcal{X}^* within a bounded error determined by $(\Delta t, K^*, \beta)$. Finally, Theorem IV.4 establishes the topological universality of the framework and demonstrates that the gradient flow remains valid for the maximal class of Genus-0 manifolds, regardless of metric distortion and boundary complexity.

V. NUMERICAL SIMULATION

To validate the effectiveness of the coverage control approach (Algorithms 1, 2, and 3), numerical simulations are conducted on the poriferous region S embedded in \mathbb{R}^3 , which is modeled as a triangular mesh with 1844 vertices.

A. Nominal Coverage Performance

In the nominal scenario, the MAS consists of $N = 6$ agents tasked with covering the poriferous region S with a non-uniform density $\rho(\theta, r) = \exp(\sin^2 \theta + \cos \theta) + 0.01r$. Based on (17), we obtain the Riemannian metric $\hat{\eta}$ of the ball world Ξ . Through conformal mapping τ , we obtain the Riemannian metric of poriferous region S . Furthermore, the length metric in Ξ and S are obtained by (18). The simulation is initialized with the parameters listed in Table I and the selection criteria for simulation parameters are provided in Appendix D. The evolution of the MAS in Ξ and S are illustrated in Fig. 3 and Fig. 4, respectively. In these snapshots, the black radial lines represent the boundaries of the sectorial partition, green stars indicate the optimal centroids c_i^* , and circles denote the current agent positions p_i . The sectorial partition boundaries successfully bypass the topological holes, ensuring each subregion remains simply connected. As shown in Fig. 5, the workload converges to an equilibrium of 1.0477 and the phase angles converge to constants. The control inputs asymptotically vanish, which confirms that the control law (19)

TABLE I
SIMULATION PARAMETERS AND CONFIGURATIONS

Symbol	Value	Physical Meaning
N	6	Total number of agents
K^*	30	Centroid tracking gain
T_ε	40	Convergence threshold
$k_{\hat{\psi}}$	0.2	Partition gain
k_p	0.12	Agent gain
β	0.005	Sequence factor

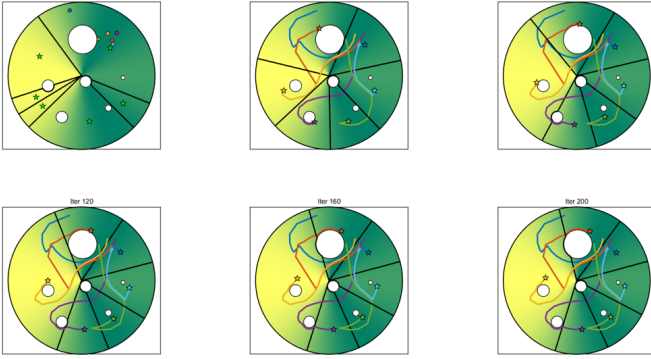


Fig. 3. Temporal evolution of the MAS in the ball world Ξ . Black radial lines denote the safe sectorial partitions, circles represent agent positions, and green stars indicate the optimal Riemannian centroids. The partition bars strictly bypass the circular obstacles, ensuring topological safety.

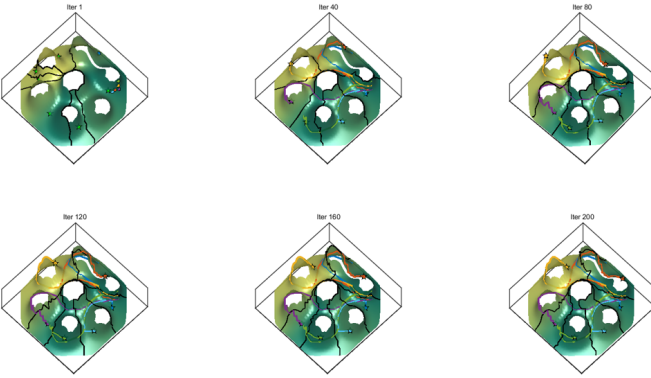


Fig. 4. Corresponding coverage evolution in the poly-annulus S . Through the inverse conformal mapping τ^{-1} , the linear sectors in Ξ are transformed into curvilinear regions in S that naturally conform to the irregular obstacle boundaries while maintaining simply connected topologies.

drives the agents to their optimal positions. According to Theorem IV.3, these positions are sufficiently close to the optimal centroids. It is worth noting that the analysis of algorithm computational complexity and the scalability of MAS is provided in Appendix E. The simulation results illustrate the effectiveness of the proposed coverage control framework.

B. Robustness under Agent Failure

To evaluate its robustness, a hardware contingency is simulated at *Iteration* = 200, where Agents 4, 5, and 6 cease operation. Upon failure, the remaining active agents \mathcal{A} must redistribute the workload previously managed by the failed agents. As shown in the latter half of Fig. 6 and Fig. 7, immediately following the failure, the partition boundaries

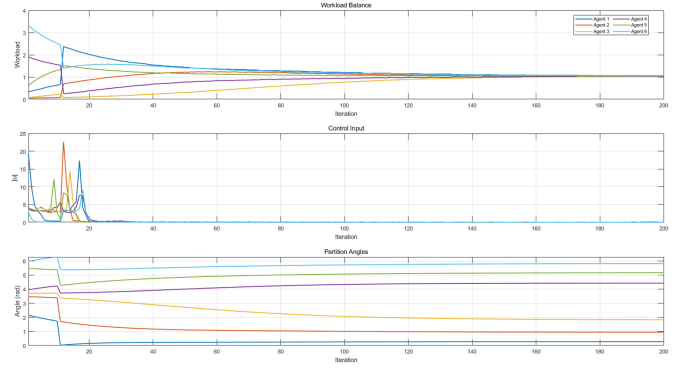


Fig. 5. Evolution of performance indices under nominal conditions: (Top) Convergence of individual agent workloads m_i to the equilibrium; (Middle) Asymptotic decay of control inputs u_i , indicating arrival at optimal centroids; (Bottom) Stabilization of partition phases ψ_i .

automatically expand to close the gap. And the coverage performance indexes under agent failures is illustrated in Fig. 8. In the normal situation, the workload converges to an equilibrium value of approximately 1.0477, and the phase angles converge to constants. The control input u for all agents asymptotically decays to zero. Following the failure of half of the agents, the workload m converges to an equilibrium value of approximately 2.0953 and the phase angles ψ also converge to constants. The control input u for all agents asymptotically decays to zero again. Although the workload per agent increases to a new equilibrium, the system maintains stability. Notably, the stability analysis of the system under agent failures is provided in Appendix E. This demonstrates that the distributed framework can autonomously re-balance the workload without requiring global reconfiguration of the conformal map τ .

The numerical performance of the proposed coverage control approach is summarized in Table II, which evaluates the system across three distinct stages: the Nominal case (nominal operation with $N = 6$), and the Pre-Fault and Post-Fault stages (contingency scenario with $N = 6$ and $N = 3$, respectively). And the indices presented include: \bar{m} (i.e., the average workload assigned to each active agent), Imbalance (i.e., the workload distribution ratio $\max(m)/\min(m)$), RMSE (i.e., the root mean square error of the workload distribution relative to the equilibrium), n (i.e., the number of convergence iterations) and t_{avg} (i.e., the average computation time per agent per iteration).

TABLE II
SUMMARY OF NUMERICAL PERFORMANCE INDICES

Scenario	\bar{m}	Imbalance	RMSE	Iters (n)	t_{avg} (s)
Nominal	1.0477	1.0017	6.75×10^{-3}	134	0.0196
Pre-Fault	1.0477	1.0016	5.91×10^{-3}	115	0.0199
Post-Fault	2.0953	1.0009	8.21×10^{-3}	76	0.0213

C. Comparison with Baseline Method

Finally, we compare the proposed approach with the Hierarchical Coverage Control (HCC) algorithm [13], which

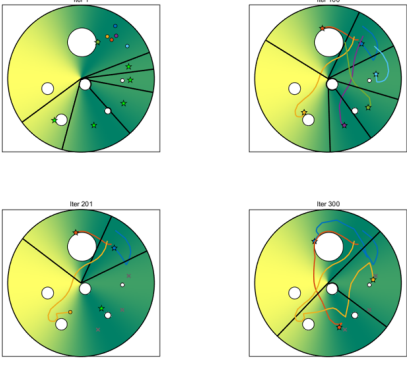


Fig. 6. Self-healing response in Ξ under agent failure at $t = 200$. The active agents autonomously expand their sectorial angles to cover the regions vacated by the failed agents, maintaining global coverage continuity.



Fig. 7. Reconfiguration of the MAS in S following agent failure. The remaining agents navigate across the manifold to redistribute the global workload, demonstrating robustness without requiring global re-mapping.

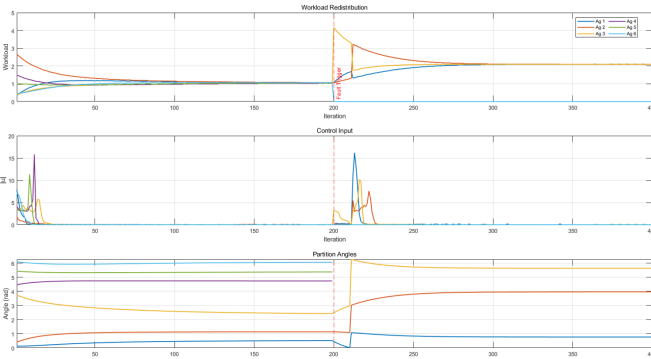


Fig. 8. Performance metrics during the failure recovery process. The dashed line at $t = 200$ marks the fault occurrence. The system exhibits a rapid transient response, where workloads m_i re-converge to a new, higher equilibrium, verifying the automatic rate compensation capability.

relies on Voronoi-based partition. As illustrated in Fig. 9, when applied to the poly-annulus manifold S , the traditional Euclidean Voronoi partition fails to account for the poriferous topology. This leads to topological disconnection, where multiple obstacles or holes are trapped within a single Voronoi cell, or a cell is split into disconnected components by a hole. Consequently, the optimal centroids fall inside obstacles or in inaccessible regions across a hole. Under these conditions, MAS models with non-holonomic constraints cannot achieve



Fig. 9. Failure case of the baseline Voronoi partition [13] on S . The metric distortion causes topological disconnection (e.g., a single cell spanned across holes), leading to unreachable centroids trapped inside obstacles.

collision avoidance or reach the assigned centroids, leading to local minima. In contrast, our sectorial partition with conformal mapping ensures that each subregion remains connected and topologically simple, effectively bypassing the inherent defects of Voronoi partition in non-convex poriferous regions.

VI. CONCLUSION

This paper developed a diffeomorphic control framework that rigorously resolved the topological obstacles inherent in multi-agent coverage on poriferous surfaces. By constructing a distributed poly-annulus conformal mapping, we established a topological conjugacy that transform arbitrary multiply-connected region into the n -holed disk. Based on the conformal mapping, the closed-loop dynamics exhibited a hierarchical convergence. The partition dynamics achieved exponential Input-to-State Stability against geometric perturbations, while the agent dynamics asymptotically converged to the optimal Riemannian centroids. Crucially, these global guarantees were achieved through a fully distributed domain decomposition to parallel partial welding, ensuring the framework's universality and scalability across a broad class of Genus-0 surfaces. Ultimately, this work proved that intricate non-convex coverage tasks could be resolved via intrinsic gradient flows on regularized coordinate systems. Future work will focus on the time-varying environments.

REFERENCES

- [1] Y. Cao, W. Ren, "Distributed coordinated tracking with reduced interaction via a variable structure approach," *IEEE Transactions on Automatic Control*, 57 (1), pp. 33-48, 2011.
- [2] A. Muzahid, S. Kamarulzaman, M. Rahman, S. Murad, M. Kamal, A. Alenezi, "Multiple vehicle cooperation and collision avoidance in automated vehicles: Survey and an AI-enabled conceptual framework," *Scientific Reports*, 603, 2023.
- [3] X. Sun, C. Cassandras, X. Meng, "Exploiting submodularity to quantify near-optimality in multi-agent coverage problems," *Automatica*, 100, pp.349-359, 2019.
- [4] M. Mesbahi and M. Egerstedt, *Graph Theoretic Methods in Multi-agent Networks*. Princeton, NJ, USA: Princeton Univ. Press, 2010.
- [5] C. Zhai, H. Zhang, G. Xiao, "Cooperative Coverage Control of Multi-Agent Systems and Its Applications," Springer-Verlag, 2021.
- [6] J. Cortes, S. Martinez, T. Karatas, F. Bullo, "Coverage control for mobile sensing networks," *IEEE Transactions on Robotics and Automation*, 20(2), pp. 243-255, 2004.

- [7] L. Pimenta, V. Kumar, R. Mesquita, G. Pereira, "Sensing and coverage for a network of heterogeneous robots", *IEEE Conference on Decision and Control*, pp. 3947-3952, 2008.
- [8] S. Bhattacharya, N. Michael, V. Kumar, "Distributed coverage and exploration in unknown nonconvex environments," *In Proceedings of the 10th International Symposium on Distributed Autonomous Robotics Systems*, pp.1-14, 2010.
- [9] S. Bhattacharya, R. Ghrist, V. Kumar, "Multi-robot coverage and exploration on Riemannian manifolds with boundaries," *International Journal of Robotics Research*, 33(1), pp.113-137, 2014.
- [10] J. Cortes, "Coverage optimization and spatial load balancing by robotic sensor networks," *IEEE Transactions on Automatic Control*, vol. 55, no. 3, pp. 749-754, 2010.
- [11] J. Palacios-Gasós, D. Tardioli, E. Montijano, C. Sagüés, "Equitable persistent coverage of non-convex environments with graph-based planning," *International Journal of Robotics Research*, 38(14), 2019.
- [12] C. Zhai, P. Fan, H. Zhang, "Sectorial coverage control with load balancing in non-convex hollow environments," *Automatica*, 2023.
- [13] J. Zou, H. -T. Zhang, C. Zhai, N. Xing, Y. Ma, X. Liu, "Cooperative Hierarchical Coverage Control of Multiagent Systems With Nonholonomic Constraints in Poriferous Environments," *IEEE Transactions on Control of Network Systems*, vol. 12, no. 2, pp. 1512-1520, 2025.
- [14] S. Surendhar, B. R. Sayan, S. Bhasin, "Distributed adaptive coverage control with obstacle avoidance for a drone network based on collective initial excitation," *Robotics and Autonomous Systems*, 2025.
- [15] X. D. Gu and S.-T. Yau, *Computational Conformal Geometry*. Beijing, China: Higher Education Press, 2008.
- [16] C. Caicedo-Nunez, M. Zefran, "Performing coverage on nonconvex domains," *2008 IEEE International Conference on Control Applications*, pp. 1019-1024, 2008.
- [17] F. Lekien, N. Leonard, "Nonuniform coverage and cartograms," *SIAM Journal on Control and Optimization*, 48(1), pp. 351-372, 2009.
- [18] P. Vlantis, C. Vrohidis, C. P. Bechlioulis and K. J. Kyriakopoulos, "Robot Navigation in Complex Workspaces Using Harmonic Maps," *IEEE International Conference on Robotics and Automation*, 2018.
- [19] L. Fan, J. Liu, W. Zhang and P. Xu, "Robot Navigation in Complex Workspaces Using Conformal Navigation Transformations," *IEEE Robotics and Automation Letters*, vol. 8, no. 1, pp. 192-199, 2023.
- [20] P. Vlantis, C. Vrohidis, C. P. Bechlioulis and K. J. Kyriakopoulos, "Navigation of Multiple Disk-Shaped Robots with Independent Goals within Obstacle-Cluttered Environments," *Sensors*, 2023.
- [21] A. Sahin and S. Bhattacharya, "Topo-Geometrically Distinct Path Computation Using Neighborhood-Augmented Graph, and Its Application to Path Planning for a Tethered Robot in 3-D," *in IEEE Transactions on Robotics*, vol. 41, pp. 20-41, 2025.
- [22] X. Xu, Y. Diaz-Mercado, "Multi-Robot Control Using Coverage Over Time-Varying Non-Convex Domains," *2020 IEEE International Conference on Robotics and Automation (ICRA)*, Paris, pp. 4536-4542, 2020.
- [23] G. Choi, "Efficient conformal parameterization of multiply-connected surfaces using quasi-conformal theory," *Journal of Scientific Computing*, 87(3), 70, 2021.
- [24] G. Notomista, G. P. T. Choi and M. Saveriano, "Reactive Robot Navigation Using Quasi-Conformal Mappings and Control Barrier Functions," *IEEE Transactions on Control Systems Technology*, 2025.
- [25] Z. Zhu, G. P. Choi, L. M. Lui, "Parallelizable global quasi-conformal parameterization of multiply connected surfaces via partial welding," *SIAM Journal on Imaging Sciences*, 15(4), 1765-1807, 2022.
- [26] L. M. Lui, K. C. Lam, T. W. Wong, X. Gu, "Texture map and video compression using Beltrami representation," *SIAM Journal on Imaging Sciences*, 6(4), 1880-1902, 2013.
- [27] P. Petersen, *Riemannian Geometry*, Springer, 2006.
- [28] P. Koebe, "Über die konforme abbildung mehrfach zusammenhängender bereiche," *Jahresbericht der Deutschen Mathematiker-Vereinigung* 19, 339-348, 1910.
- [29] F. Wolter, "Cut loci in bordered and unbordered Riemannian manifolds," PhD thesis, Technical University of Berlin, 1985.
- [30] H. K. Khalil, *Nonlinear Systems*, 3rd ed. Upper Saddle River, NJ, USA: Prentice Hall, 2002.
- [31] R. A. Horn and C. R. Johnson, *Matrix Analysis*, 2nd ed. Cambridge, U.K. Cambridge Univ. Press, 2013.
- [32] P.-A. Absil, R. Mahony and R. Sepulchre, *Optimization Algorithms on Matrix Manifolds*. Princeton, NJ, USA: Princeton Univ. Press, 2008.
- [33] N. Boumal, *An Introduction to Optimization on Smooth Manifolds*. Cambridge, UK: Cambridge Univ. Press, 2023.
- [34] S. Bonnabel, "Stochastic gradient descent on Riemannian manifolds," *IEEE Transaction Automatic Control*, vol. 58, no. 9, 2013.

APPENDIX A PARTIAL WELDING EXAMPLE

To illustrate the mathematical mechanism of partial welding, we present a intuitive example. Reconstruct the topological connectivity of a slit domain $\mathcal{D} = \mathbb{C} \setminus [-i, i]$ by welding its separated boundaries. Let the slit $[-i, i]$ be regarded as two distinct boundary segments: $\gamma^+ = \{iy + \epsilon \mid y \in [-1, 1]\}$, and $\gamma^- = \{iy - \epsilon \mid y \in [-1, 1]\}$, where $\epsilon \rightarrow 0^+$. The welding mapping $T : \mathcal{D} \rightarrow \Omega$ is defined by the elementary function $w = T(z) = \sqrt{z^2 + 1}$. This mapping transforms the slit domain \mathcal{D} into the $\Omega = \mathbb{C} \setminus (-\infty, 0]$. Crucially, it enforces the boundary identification condition:

$$T(iy^+) = T(iy^-) = \sqrt{1 - y^2}, \quad \forall y \in [-1, 1]. \quad (27)$$

This implies that the disjoint banks γ^+ and γ^- are mapped to the exact same locus in Ω , thereby welding the cut back together. In our proposed framework, the optimization of Θ_{uv} (8))serves as the numerical inverse operator of such welding. It explicitly identifies the boundary correspondence:

$$h_u(\partial S_u) \cong \Theta_{uv}(h_v(\partial S_v)), \quad (28)$$

which effectively restoring the continuous topology of poly-annulus S from the decomposed local disks.

APPENDIX B GEOMETRIC COMPUTATION OF SAFE BOUNDARY

This appendix details the numerical generation of the partition bar $\hat{\Gamma}_i$ in Ξ , consisting of linear segments and circular arcs. For intersection identification, the i -th nominal partition bar is parameterized as a vector $\hat{\mathbf{x}}(\hat{\xi}) = \hat{\xi} \hat{\mathbf{b}}_i$, where $\hat{\xi} \in [0, 1]$. The k -th obstacle is defined by its center \hat{o}_k and radius \hat{r}_k . The intersection points are determined by the Euclidean constraint $\|\hat{\mathbf{x}}(\hat{\xi}) - \hat{o}_k\|^2 = \hat{r}_k^2$, which yields the quadratic equation:

$$|\hat{\mathbf{b}}_i|^2 \hat{\xi}^2 - 2(\hat{\mathbf{b}}_i \cdot \hat{o}_k) \hat{\xi} + (|\hat{o}_k|^2 - \hat{r}_k^2) = 0. \quad (29)$$

Solving for $\hat{\xi}$ gives the entry and exit parameters $\hat{\xi}_{in} < \hat{\xi}_{out}$, with corresponding coordinates $\hat{p}_{in} = \hat{\xi}_{in} \hat{\mathbf{b}}_i$ and $\hat{p}_{out} = \hat{\xi}_{out} \hat{\mathbf{b}}_i$. To bypass the obstacle, a circular arc is generated on the buffer circle with radius $\hat{r}_{k,i} = \hat{r}_k(1 + i\beta)$. The entry and exit angles relative to \hat{o}_k are computed as $\hat{\psi}_{in} = \text{atan2}(\hat{p}_{in} - \hat{o}_k)$ and $\hat{\psi}_{out} = \text{atan2}(\hat{p}_{out} - \hat{o}_k)$. The safe arc $\hat{A}_{k,i}$ is then discretized via angular interpolation:

$$\hat{\mathbf{x}}_{arc}(u) = \hat{o}_k + \hat{r}_{k,i} \begin{bmatrix} \cos(\hat{\psi}_{in} + u \frac{\Delta \hat{\psi}}{U-1}) \\ \sin(\hat{\psi}_{in} + u \frac{\Delta \hat{\psi}}{U-1}) \end{bmatrix}, \quad (30)$$

where $u \in \{0, \dots, U-1\}$. This ensures $\hat{\Gamma}_i$ is piecewise smooth and strictly disjoint from obstacles.

APPENDIX C SPECTRAL PROPERTIES OF $\mathcal{L}_G(\hat{\omega})$

For the weighted Laplacian $\mathcal{L}_G(\hat{\omega})$ defined in (21), under $\hat{\omega}_k \geq \underline{\omega} > 0, \forall k \in \mathcal{N}$, the properties hold:

- 1) $\mathcal{L}_G = \mathcal{L}_G^T$ and $\mathcal{L}_G \succeq 0$.
- 2) $\ker(\mathcal{L}_G) = \text{span}(\mathbf{1}_N)$, implying $\sum_{i=1}^N \hat{m}_i = 0$.
- 3) $\lambda_2(\mathcal{L}_G) \geq \underline{\omega} \lambda_2(\mathcal{L}_S) = 2\underline{\omega}(1 - \cos(2\pi/N)) > 0$.

Proof. Positive Semi-definiteness: Symmetry follows from the undirected adjacency in \mathcal{G}_N . For any $x \in \mathbb{R}^N$, the quadratic form is $x^T \mathcal{L}_G x = \sum_{k=1}^N \hat{\omega}_k (x_k - x_{k-1})^2 \geq 0$, where $x_0 \equiv x_N$. Then, $\mathcal{L}_G \succeq 0$. Null Space: $x^T \mathcal{L}_G x = 0 \iff x_k = x_{k-1}$ for all k . Hence, $\ker(\mathcal{L}_G) = \text{span}(\mathbf{1}_N)$. Connectivity: Since $\underline{\omega} > 0$, the cycle graph \mathcal{G}_N is connected. By the Courant-Fischer Theorem [31, Th. 4.2.2], the second smallest eigenvalue satisfies $\lambda_2(\mathcal{L}_G) \geq \underline{\omega} \lambda_2(\mathcal{L}_S) > 0$, which establishes the exponential stability on the subspace $\mathbf{1}_N^\perp$. \square

APPENDIX D PARAMETERS DESIGN

The centroid tracking gain K^* and agent gain k_p are tuned to ensure that agents navigate poly-annulus S toward their respective centroids, while strictly adhering to the Riemannian metric constraints. The partition gain $k_{\hat{\psi}}$ is determined by the spectral properties of the communication topology to guarantee the exponential decay of workload imbalances across the multi-agents. To maintain topological connectivity in the presence of holes, the sequence factor β is introduced, which ensures that the obstacle-avoiding partition bars remain disjoint and strictly separated from the boundary components in Ξ . Finally, the convergence threshold T_ε is calibrated to define the steady-state precision of the coverage mission, ensuring the terminal configuration satisfies the quasi-optimal workload distribution.

APPENDIX E ALGORITHM ANALYSIS

This section evaluates the computational efficiency, scalability and robustness of the proposed diffeomorphic coverage control framework.

A. Computational Complexity

The framework decouples offline mapping from online distributed execution to ensure real-time performance:

- 1) Mapping (Algorithm 1): Solving the Laplace equation for the conformal map τ on S with v vertices across M subdomains incurs a complexity of $O((V \cdot M^{-1})^{1.5})$.
- 2) Partition (Algorithm 2): The linear intersection checks between N partition bars and n obstacles yield a complexity of $O(n)$ per control cycle.
- 3) Control (Algorithm 3): Each iteration involves $O(D_{\mathcal{G}})$ communication rounds, where $D_{\mathcal{G}}$ is the graph diameter.

The total online complexity is $O(n + K^* \cdot D_{\mathcal{G}})$. As shown in Table II, the average execution time $t_{avg} \approx 0.02$ s per agent, supporting high-frequency deployment.

B. Scalability Analysis

The poriferous geometry of S imposes a theoretical limit on the agent population N to maintain topological disjointness and ISS stability. Given a sequence factor β , the maximal agent capacity N_{max} is determined by:

$$N_{max} \leq \min\{0.5\hat{d}_{min} \cdot (\hat{r}_{max}\beta)^{-1}, \gamma\epsilon_{max} \cdot (C_{\hat{\delta}}\beta)^{-1}\}, \quad (31)$$

where \hat{d}_{min} is the minimum obstacle separation, \hat{r}_{max} is the maximum obstacle radius, and ϵ_{max} is the allowable workload error. The first term in (31) ensures the non-overlapping of buffer zones $(\hat{r}_k(1 + N\beta) - \hat{r}_k \leq 0.5\hat{d}_{min})$, while the second term guarantees the ultimate workload error $\|\mathbf{e}(\infty)\| \leq C_{\hat{\delta}}\beta \cdot \gamma^{-1}$ remains within ϵ_{max} , where $C_{\hat{\delta}}$ is the geometric sensitivity defined in Lemma IV.1. This bound defines the fundamental trade-off between coverage precision β and the swarm scale N on poly annulus S .

C. Robustness Analysis

Consider a failure at $t = T_f$ where a subset of agents $N_{\mathcal{F}}$ ceases operation, resulting in an active set \mathcal{A} with size $N_{\mathcal{A}} = N - N_{\mathcal{F}}$. Then, the new equilibrium workload is $\bar{m}_{\mathcal{A}} = M_{total} \cdot N_{\mathcal{A}}^{-1}$. Define the error vector $\mathbf{e} \in \mathbb{R}^{N_{\mathcal{A}}}$ with components $e_i = \hat{m}_i - \bar{m}_{\mathcal{A}}$, satisfying $\mathbf{e} \perp \mathbf{1}_{N_{\mathcal{A}}}$. Under the reduced topology, the error dynamics in Ξ follow the Riemannian Laplacian flow $\dot{\mathbf{e}} = -k_{\hat{\psi}} \mathcal{L}_G(\hat{\omega}) \mathbf{e}$, where $\mathcal{L}_G(\hat{\omega})$ is the weighted Laplacian induced by the metric $\hat{\eta}$. For $V = \|\mathbf{e}\|^2/2$, its derivative satisfies

$$\dot{V} = -k_{\hat{\psi}} \mathbf{e}^T \mathcal{L}_G(\hat{\omega}) \mathbf{e} \leq -k_{\hat{\psi}} \cdot \underline{\omega} \cdot \lambda_2(\mathcal{L}_{S, N_{\mathcal{A}}}) \cdot \|\mathbf{e}\|^2, \quad (32)$$

where $\underline{\omega} > 0$ is the minimum marginal density. The exponential convergence rate is $\gamma_{\mathcal{A}} = 2k_{\hat{\psi}} \cdot \underline{\omega} \cdot (1 - \cos(2\pi \cdot N_{\mathcal{A}}^{-1}))$. Since $N_{\mathcal{A}} < N$, the spectral property of the cycle graph ensures $\gamma_{\mathcal{A}} > \gamma_{\mathcal{N}}$. The system's re-balancing speed automatically increases as the swarm size reduces, ensuring that the error $\|\mathbf{e}(t)\| \leq \|\mathbf{e}(T_0)\| \exp(-\gamma_{\mathcal{A}}(t - T_f))$ swiftly decays. This intrinsic self-healing property allows the remaining agents to reach new Riemannian centroids without manual reconfiguration of the map τ or the Riemannian metric $\hat{\eta}$.